Hyperspectral AO Observations of Solar System Objects

J.J. Hillman[1], D.A. Glenar[1], G. Chin[1], N.J. Chanover[2], W.E. Blass[3], S.L. Mahan[3], M. Le Louarn[4]

[1]NASA's Goddard Space Flight Center, Greenbelt
[2]New Mexico State University, Los Cruces
[3]University of Tennessee, Knoxville
[4]ESO, Garching

Abstract

We describe planetary science observations made with the Goddard Space Flight Center, acousto-optic tunable filter (AOTF) camera. This camera is a newly developed RF-tunable spectrophotometric imager with a spectral bandwidth of 25 cm^{-1} and a tuning range from0.5 to 1.0 micron. The observations that we report here were made at the Starfire Optical Range 1.5-meter laser-beacon adaptive optics telescope facility. Observations of Jupiter and Saturn are reported. The superior spectral resolution of the AOTF camera was exploited to image these objects both in and out of molecular absorption bands, allowing us to sound to different depths in their respective atmospheres. The Jupiter and some of the Saturn observations were made during the Comet Shoemaker-Levy 9 collisions in July 1994. Saturn (and Titan) was observed again in September 1995. The enhanced spatial resolution offered by the adaptive optics facility allowed us to observe cloud and storm activity in the atmospheres of Jupiter and Saturn that are not normally observable with conventional ground-based telescopes. In this paper we will emphasize post-observation data processing including the determination of point-spread-function and deconvolution techniques to enhance the collected images. Our newest AOTF camera operates in the near-IR, 1.7-3.4 micron (Chanover *et al*. 1998). We will discuss future plans to use this camera at an adaptive optics facility, in a coordinated observing campaign in support of the Mars Global Surveyor mission.

1. Instrumentation

Because of several unique aspects of our AOTF camera, it is appropriate to discuss this technology here. The theory of operation of non-collinear AOTFs has been reviewed by Glenar *et al.* 1994. Tellurium dioxide (TeO_2) is the most mature AOTF material, and the best choice for operation at wavelengths in the 0.5-5.0 micron region (Katzka 1987). The AOTF crystal is both birefringent and electro-optic. A RF acoustic wave is applied to the crystal. This sets up an internal phase grating by modulating the index of refraction. Each linear polarization state of the incoming light is diffracted into the opposite state and deflected upon exit from the crystal if its wavelength satisfies a specific momentum matching condition, $k_d = k_i \pm k_a$. To employ this filter in a camera concept, broadband, randomly polarized light is allowed to enter the AOTF crystal and the acousto-optic interaction causes a single wavelength to be divided into two polarization states which are symmetrically deflected at the output. These beams can be individually refocused into two monochromatic polarized images. Tuning is accomplished by changing the applied RF frequency. Figure 1 shows the optical design of our AOTF camera. The foreoptics consist of a 5 mm x 6 mm input field stop and a field lens which reimages the telescope exit pupil onto a stop. The relay lenses reimage the field at 1:1 magnification near the AOTF

input. A second field lens is placed here in order to image the pupil stop at infinity. This guarantees telecentricity, i.e. all of the light stays within a minimum divergence cone as it passes through the AOTF. This configuration allows the instrument to operate with telescopes as "fast" as ~f/12 without loss of diffraction efficiency or spectral smearing. Note also that no physical stop is placed at the AOTF input where it can scatter or diffract light at extreme angles. Careful suppression of stray light is important in an AOTF instrument, because a very small fraction of the broadband undiffracted light can contaminate the narrow-band diffracted images, and make accurate flat-fielding impossible. Upon exit from the AOTF, the orthogonally polarized beams are collimated and reimaged side-by-side on a rectangular CCD array. More complete details of this configuration can be found in Glenar *et al.* 1997.

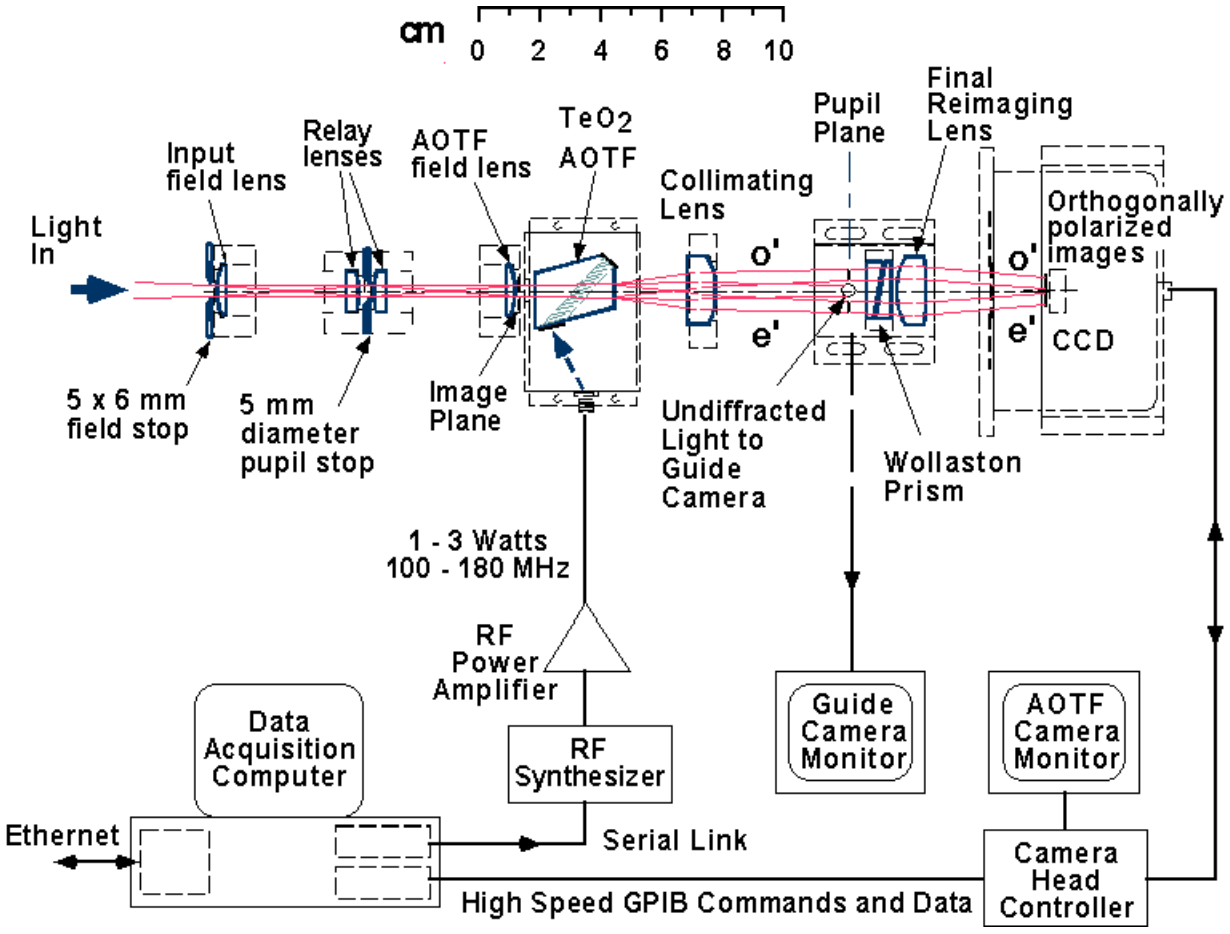

Fig. 1 – Optical design of the AOTF Camera and block diagram of the data acquisition setup used at the Starfire Optical Range, 1.5-m Laser Beacon Facility.

2. Observations

As stated above, our observations were made at the Starfire Optical Range (SOR) in Albuquerque, NM, a Rayleigh beacon adaptive optics facility operated jointly by the Phillips Laboratory and Kirtland AFB.

A full discussion of this telescope facility has been published (Fugate *et al.* 1994).

The laser beacon at the SOR 1.5-meter telescope consists of a 180 W average power pulsed copper vapor laser with a pulse rate of 5-kHz and 50-nsec pulse duration. The midpoint focus altitude is approximately 10-km with a 2.4-km range-gate. For our observing sessions the telescope was configured for tip-tilt stabilization on extended objects (planets) using a 14 x 14 Ge detector array and servo loop capable of rapid (>300-Hz bandwidth) object centroiding. We employed an image correlation processor instead of the usual image centroid algorithm. This processor was more effective for Saturn than for Jupiter, which overfilled the track gate. This fast full-disk correlator was used for tip-tilt aperture correction while the laser beacon was used for high order phase correction across the telescope aperture.

The quality of this correction is largely limited by focus anisoplanatism arising from the finite focus altitude. This limitation leads to a parametric model for our point-spread-function, which is discussed in the following Section. The phase correction also depends on atmospheric parameters including the Fried parameter r_o, which is closely related to the horizontal atmospheric coherence length, with observed values in 10- to 15-cm range during clear nights, and on the Greenwood frequency which represents the atmospheric coherence time.

The science focal plane was shared between a broadband CCD camera at a scale of 0.089 arcsec/px for evaluating image quality and our AOTF camera. Using images of ϑSer, a double star with a separation of 22.3 arcsec, we measure a plate scale of 0.159 arcsec/px for the AOTF camera. This spatial resolution and a focal ratio of f/20 represent a balance between the sensitivity limitations set by very-narrow-band imaging and the need to have the spatial sampling approach the diffraction limit.

For the AOTF crystal installed in the camera used in these observations we measure full-width-half-maximum of 29 cm^{-1} corresponding to a resolving power, $\lambda/\Delta\lambda = 430$ at 800 nm. For outer planet measurements this permits well defined vertical sounding of the atmosphere by alternately imaging at the center of CH_4 bands and adjacent continua. Because these absorption bands have different strengths, images taken at these wavelengths probe a range of altitudes in the atmosphere. For the Jupiter observations our band-center wavelengths were 887-, 897-, 725-, 790-, 760- and 825 nm. Passband-averaged methane absorption coefficients at these center wavelengths result in weighting functions (the gradient of the transmittance through the atmosphere) which have peaks in pressure regions from the lower stratosphere (887 nm) down to the cloud tops (825 nm).

3. Post-Observation Processing

AOTF cameras are subject to stray light contamination due to the small deflection angles inherent in these devices. Hence, each observation consists of two successive, equal integrations, the first with the AOTF operating (RF on) and the second with it switched off. Likewise, a flatfield reference at each wavelength using the closed telescope dome consisted of successive on/off integration periods. Defining SL_{src} and SL_d as the stray light from source and dome flat, G_{xy} the electronic camera gain and Z the zero level which includes CCD dark current and bias, a flatfielded result consists of

$$\text{Flatfield Image} = \frac{[(Source + Sky + SL_{src})G_{xy} + Z] - [SL_{src}G_{xy} + Z]}{[(Domeflat + SL_d)G_{xy} + Z] - [SL_dG_{xy} + Z]}$$

Which reduces to

$$\text{Flatfield Image} = \frac{Source + Sky}{Domeflat}$$

Sky subtraction was accomplished by constructing histograms of the scene near the planet in each flatfielded image and then subtracting the derived mean value from the entire image.

Flatfielded AOTF images were then converted to absolute I/F at each wavelength using measurements of a nearby photometric-standard star 109Vir, which has been calibrated by Oke 1964 and later Tug et al. 1977. Solar irradiance at Jupiter was obtained using measurements of the solar spectrum (Necke and Labs 1984). The absolute reflectance I/F_{px} at each pixel and at each wavelength is given by

$$\frac{I}{F_{px}} = \frac{F^*}{\sum \Phi^*} \frac{\pi}{\pi F_s} \frac{\Phi_{pxJ}}{\Omega_{px}} \frac{\tau^*}{\tau_J} 10^{-k_\lambda (AM^* - AM_J)/2.5}$$

Where F^* is the calibration star flux in photons $cm^{-2}sec^{-1}nm^{-1}$, $\Sigma\Phi^*$ is the spatially integrated star signal, πF_s is the solar irradiance at Jupiter in photons $cm^{-2}sec^{-1}sterad^{-1}nm^{-1}$, Ω_{px} is the solid angle subtended by a pixel, Φ_{pxJ} is the Jupiter signal appearing on one pixel, τ^* and τ_J are the star and planet integration times, AM^* and AM_J are the object airmasses and k_λ is the atmospheric extinction coefficient in mag $airmass^{-1}$.

3.1 Deconvolution

After flatfielding and photometric calibration the images were enhanced using a technique developed by Chin, Blass and Mahan for the analysis of HST images (Chin *et al*. 1994; Blass *et al*. 1995) and referred to herein as the CBM method. This process permits the direct recovery of an estimator of the object Θ given the point-spread-function (PSF) p and the observed image I, where

$$I = p \otimes \Theta$$

In practice, this process involves recovering a mapping function q from

$$T = p \otimes q$$

where T is the target function into which it is desired to map the PSF p. The CBM method recovers the mapping function q given p and T. The enhanced imaging process is then represented as

$$I \otimes q = (p \otimes q \otimes \Theta) = T \otimes \Theta.$$

The enhanced image is $T \otimes \Theta$. In practice T is taken as a narrow Gaussian function. CBM is used to construct a mapping function q such that p is mapped to T. The mapping function is then convolved

with the image I to better approximate the true object Θ. If the target T were a delta-function (not possible in practice due to Nyquist sampling requirement and the presence of noise) the mapped estimator of Θ, i.e. T⊗Θ, would be the object itself.

In order to generate the mapping function q a good approximation for the PSF is necessary. One limitation of AO is that any post-observing improvement of the PSF by deconvolution requires a small (or point) object in the field during the measurements in order to estimate the PSF.

3.2 Parametric Point-Spread-Function

Due to the effects of focus anisoplanatism the PSF was approximated (Northcott and Roddier 1994) as the sum of a near-diffraction limited Gaussian core representing the AO-corrected portion (up to the focus altitude) and a broad, long exposure pedestal representing the uncorrected "seeing" portion (Molina and Ripley 1989),

$$p(r) = (1-a)e^{-(r/w_c)^2} + a\left(1+\left(r/w_p\right)^2\right)^{-3}$$

In the case of the Jupiter images, a PSF was determined from an observed shadow of the satellite Ganymede on the Jovian cloud-tops seen in one of the images (see Fig. 2). By iteratively convolving

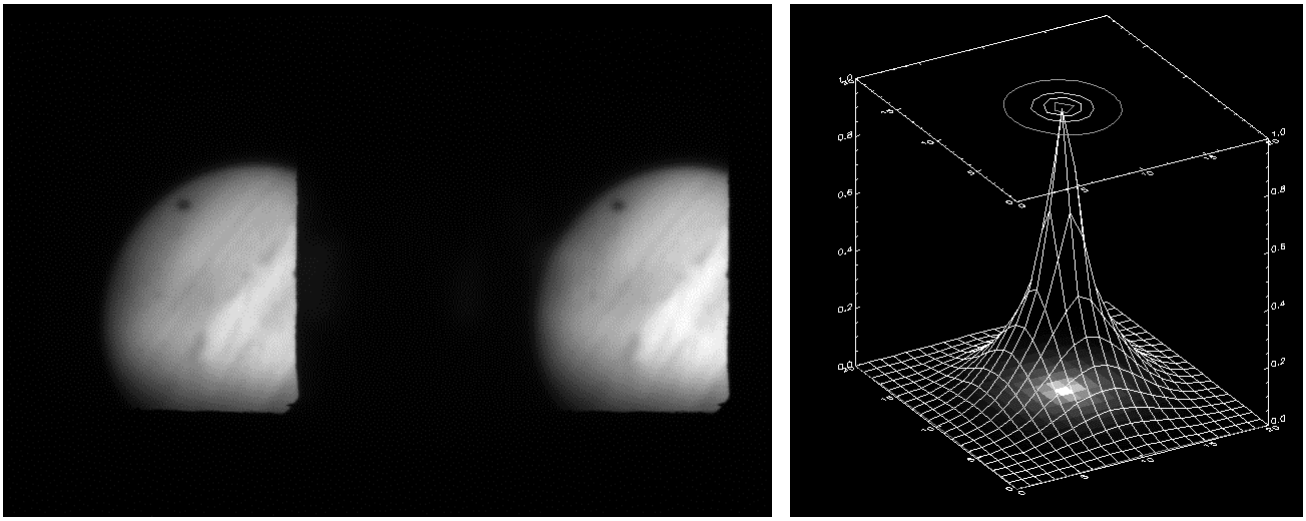

Fig. 2 – Two orthogonal linear polarization images of the Ganymede shadow taken at 825 nm are shown on the left. The right image shows a wire-frame surface map of the PSF derived from the Ganymede-shadow model.

our model PSF with the geometric Ganymede shadow, the result could be brought into agreement with the observation by varying three parameters, the pedestal amplitude a, the pedestal width w_p and the core width w_c. We obtained a core FWHM of 0.32 arcsec, pedestal FWHM 1.3 arcsec and pedestal amplitude of 0.35. These derived widths may be compared to limiting-case estimates. In the diffraction limit the core FWHM may be approximated by λ/D. For the 1.5-m telescope at a wavelength of 825 nm, the band where the shadow was seen we obtain λ/D≈ 0.66 μrad or 0.14 arcsec. Our measured PSF has a core width approximately a factor of two larger than this limiting value. The pedestal width has a

limiting value set by the atmospheric coherence length or λ/r_o. Our detailed observing log shows that for the Ganymede-shadow-observations r_o was 15 cm. We obtain a limiting value of $w_p \approx 5.5$ μrad or 1.1 arcsec. Our measured value of 1.3 arcsec agrees very well with this.

Using this result, the mapping function q was determined and used to deconvolve the entire Jupiter AOTF data set. Figure 3 (on following page) shows the effect of decreasing the target width T. The upper left image is an image taken at 887 nm, the strongest methane band and therefore peaking highest in altitude. At this altitude the stratospheric polar haze is visible and the comet collision sites appear brighter than the underlying cloud tops. This image has not been deconvolved using the CBM method. In the subsequent images the target width T is reduced from 5.0 to 3.0 in units of 0.5 pixels. One observes a gradual increase in sharpness of core-corrected image and a gradual decrease in signal-to-noise ratio. Using a value of T=4.0 based on the observed signal-to-noise ratio we show a complete 6-wavelength image cube of deconvolved Jupiter data in Fig. 4 (on following page). The 825 nm image affords us the best view of the cloud tops since the methane absorption coefficient is lowest in this band. In all of these images one sees the H-collision site near the central meridian and the combined G- and D-collision sites near the terminator.

In the case of Saturn observations we used the icy satellite Rhea to obtain an estimate of the PSF. Rhea, a 765-km diameter satellite subtends an angular size of 0.235 arcsec or 2.66 px diameter. This flattop model was iteratively convolved with our model PSF until agreement with observations was achieved (see Fig. 5). Best fit was achieved with a Gaussian core FWHM of 0.29 arcsec.

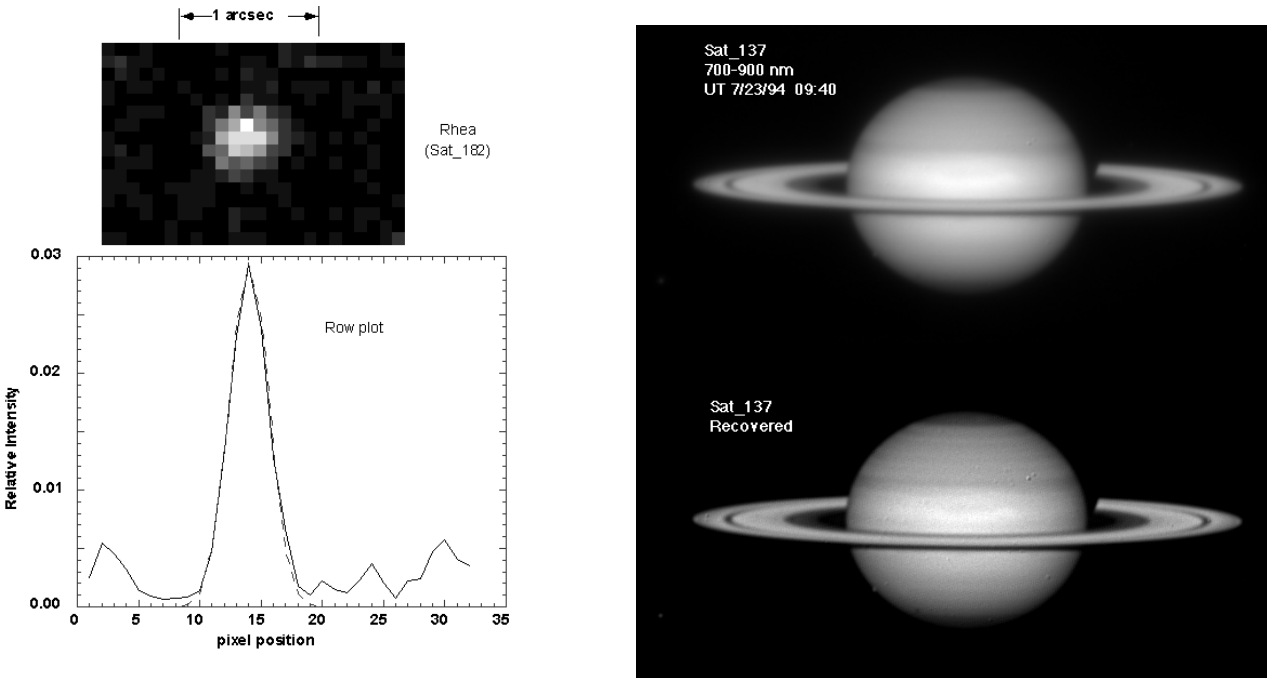

Fig. 5 – The raw image of Rhea and subsequently derived PSF are shown on the left. On the right we show a raw Saturn image and below it a recovered image using the CBM method.

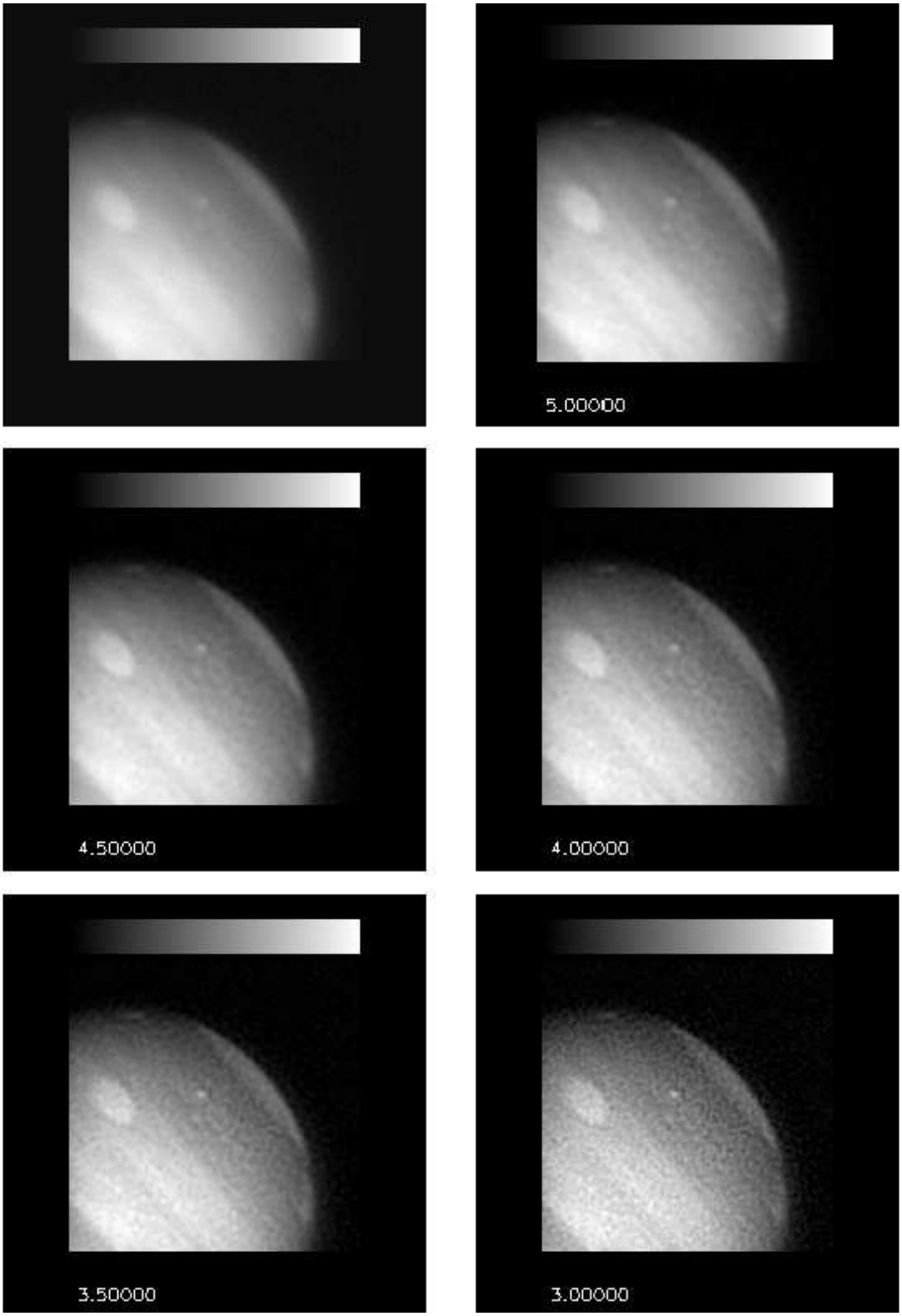

Fig. 3 - The upper left image is an image taken at 887 nm, the strongest methane band and therefore peaking highest in altitude. This image has not been deconvolved using the CBM method. In the subsequent images the target width T is reduced from 5.0 to 3.0 in units of 0.5 pixels. One observes a gradual increase in sharpness of core-corrected image and a gradual decrease in signal-to-noise ratio.

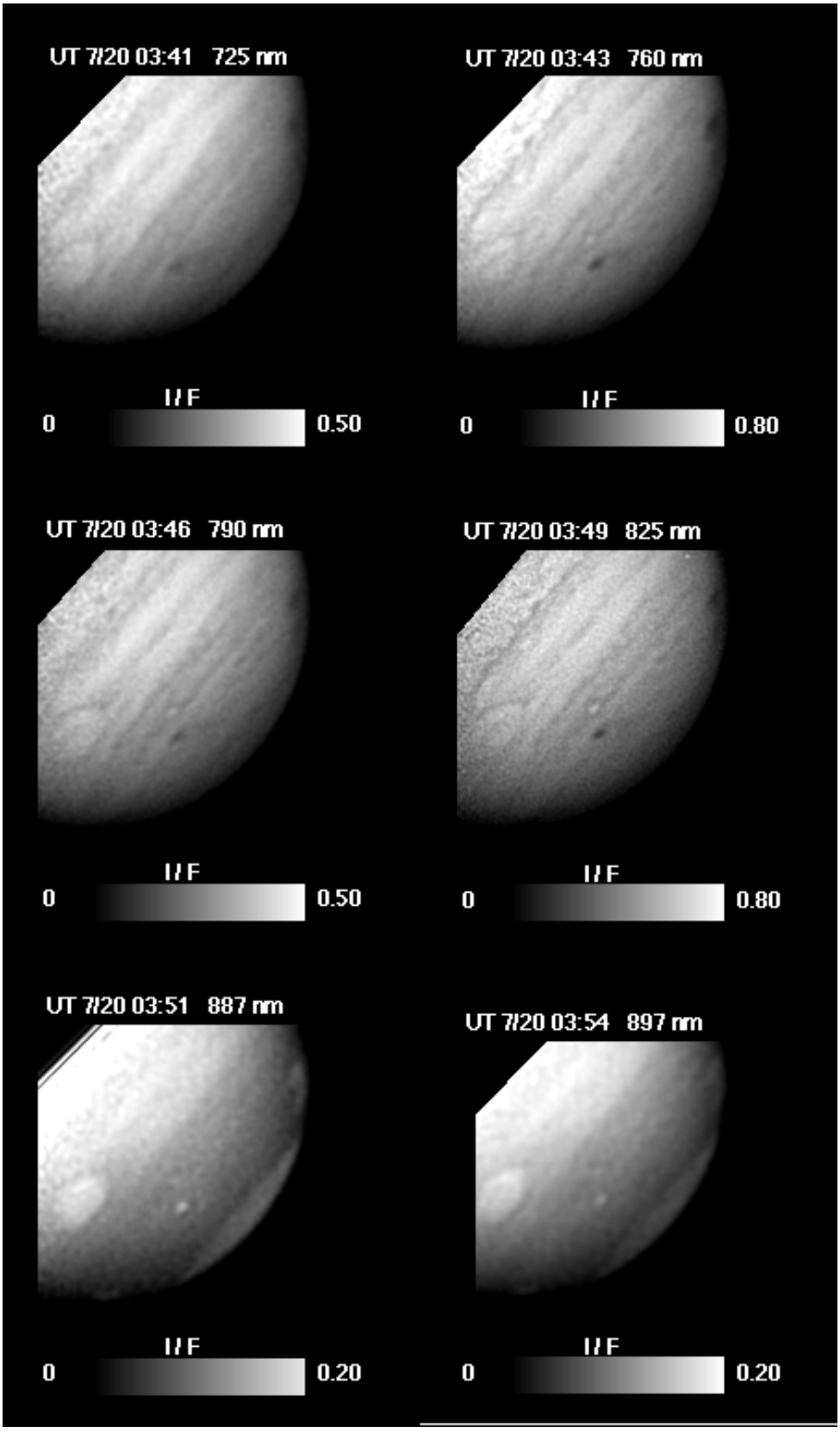

Fig. 4 – A complete image-cube of deconvolved Jupiter images is shown. The CBM method was employed with a target value of T=4.0 based on the data of figure 3.

4. Summary & Conclusions

With these measurements we have demonstrated the combined use of AOTF imaging spectroscopy with laser-beacon adaptive optics on spatially extended sources. High spatial and spectral resolution images of Jupiter and Saturn were obtained and the details of photometric calibration and deconvolution of PSF were presented. We have shown that using adaptive optics shortward of 1-micron enables a large improvement in spatial resolution compared to conventional ground based telescopes. Due to focus anisoplanatism and the extended source size we used a PSF model that included both corrected and uncorrected components. This resulted in a best-case Strehl ratio of about 0.23. In spite of these limitations, subsequent deconvolution yielded a spatial resolution of better than 0.3 arcsec over the entire field of view, which in the case of Saturn extended over the full disk and rings.

The AOTF camera allows us to image at any wavelength with a spectral resolution several times that of fixed interference filters. By its nature, this camera generates simultaneous images in two orthogonal linear polarizations. This may prove useful in some astrophysical applications.

An observing Campaign is being formed for the Mars opposition, which occurs in late April 1999. Our objective is to assemble a photometrically calibrated, spectrally complete ground-based image cube at the highest possible spatial resolution. These measurements will employ new observing technologies and will be concurrent both with Mars Global Surveyor spacecraft measurements and supporting observations by the upgraded HST. Three observing teams will conduct the investigations with 3 instruments spanning 0.6 to 5.0 micron. The instruments and planned observing facilities are: (a) Visible/NIR AOTF camera will be employed at USAF/Phillips Lab 1.5m, laser-beacon adaptive optics telescope. Auxiliary camera with interference filter wheel. 600-1050 nm. ~0.3 arcsec (125 km). Science targets: Fe2+, Fe3+ mineralogy and coarse grain hematite search. (b) SWIR AOTF camera at Apache Point Observatory, 3.5m, f/10, Nasymth focus. 1.7-3.4 micron (AOTF limited). 0.8 arcsec (340 km). Science targets: 3 micron water-of hydration feature and CO2, H2O ice (polar regions and clouds). (c) KPNO cryogenic grating/slit spectrometer (CRSP/SALLY) at KPNO 2.1 m, f/15 Cass. focus. Selected 3-5 micron (L, M band). ~1.2 arcsec Nyquist (500 km). Science targets: Water-of-hydration (3-4 micron long wave extension) and sulfate mineralogy.

Acknowledgement

We are very grateful to the members of SOR Technical Staff and in particular would like to thank Drs. Robert Fugate and Jack Drummond for their great help during our several observing runs. We thank C. Peruso, W. Schaefer and R. Oliverson for supporting the instrument testing. NASA's Planetary Instrument Definition and Development Program and the GSFC Director's Discretionary Fund provided support for these observations.

References

Blass, W. E., S. L. Mahan and G. Chin, Convolution connection paradigm neural network enables linear system theory based image enhancement, *Int. J. Imaging Sys. & Tech. 6,* 350-357 (1995).

Chanover, N. J., D. A. Glenar and J. J. Hillman, Multispectral near-IR imaging of Venus night side cloud features, *J. Geophys. Res.* in press (1998).

Chin, G, S. L. Mahan and W. E. Blass, Numerical solutions for convolution equations: Applications of a novel neural network, *The Restoration of HST Images and Spectra – II,* R. J. Hanish and R. L. White, eds., Proceedings of a workshop held at STScI, Baltimore, MD (1993).

Fugate, R. Q., et al., Two generations of laser-guide-star adaptive-optics experiments at the Starfire Optical Range, *J. Opt. Soc. Am. A 11,* 301-314 (1994).

Glenar, D. A., J. J. Hillman, B. Saif and J. Bergstralh, Acousto-optic imaging spectropolarimetry for remote sensing, *Applied Optics 33,* 7412-7424 (1994).

Glenar, D. A., J. J. Hillman, M. LeLouarn, R. Q. Fugate and J. D. Drummond, Multispectral Imagery of Jupiter and Saturn using Adaptive Optics and Acousto-Optic Tuning, *Pub. Astron. Soc. Pacific 109,* 326-337 (1997).

Katzka, P., AOTF overview: past, present and future, in Acousto-optic, Electro-optic and Magneto-optic Devices and Applications, J. A. Lucero, ed. *Proc. Soc. Photo-Opt. Instrum. Eng. 753,* 22-28 (1987).

Molina, R. and B. D. Ripley, Using spatial models as priors in astronomical image analysis*, J. Appl. Statist. 16*, 193-206 (1989).

Neckel, H. and D. Labs, The solar radiation between 3300A and 12500A, *Solar Phys. 90,*205-258 (1984).

Northcott, M. J. and C. Roddier, Adaptive optics at the University of Hawaii III: the adaptive optical PSF, *Proc. Soc. Photo-Opt. Instrum. Eng. 2201,* 129-136 (1994).

Oke, J. B., Photoelectric spectrophotometry of stars suitable for standards, *Astrophys. J 140,* 689-693 (1964).

Tug, H., N. M. White and G. W. Lockwood, Absolute energy distributions of α Lyrae and 109 Virginis from 3295A to 9040A, *Astron. Astrophys 61,* 679-684 (1977).